

Automated 3D Tumor Reconstruction and Breast Cancer Detection Using Deep Learning with Secure Data Handling

Manasa Sandeep^{1*}, and Dr.C. Nandini²

^{1*}Department of Computer Science and Engineering, Dayananda Sagar Academy of Technology and Management, Bengaluru, Karnataka, India; Visvesvaraya Technological University, Belagavi, Karnataka, India. vmansa18@gmail.com, <https://orcid.org/0009-0000-4560-2361>

²Department of Computer Science and Engineering, Dayananda Sagar Academy of Technology and Management, Bengaluru, Karnataka, India; Visvesvaraya Technological University, Belagavi, Karnataka, India. hodcse@dsatm.edu.in, <https://orcid.org/0000-0001-9350-0220>

Received: October 18, 2025; Revised: November 26, 2025; Accepted: January 16, 2026; Published: February 27, 2026

Abstract

Breast Cancer (BC) is the most diagnosed and the second most frequent cause of death among women. Despite the wide application of mammography as a screening technique, the low sensitivity of this technique in dense breasts, and the risks of radiation are significant disadvantages. In diagnosing and early treatment planning of breast cancer, medical imaging is very important. This paper provides a framework for the segmentation and 3D reconstruction of breast tumors based on a 3D NIFTI image dataset. The preprocessing step entails using an integration of Non-Local Means (NLM) filter and Sobel edge detector to effectively minimize noise and maintain significant structure of the breast tissue. Among the three deep learning models, including UNet, ResNet, and a hybrid architecture of UNet-ResNet, the segmentation of tumor regions is carried out. These models are tested on traditional measures such as Dice Coefficient and Jaccard Index, with the hybrid UNet-ResNet model performing better than others, with a Dice coefficient of 1.38 and a Jaccard index of 0.08. After the segmentation, the volume of the tumor is estimated through the spatial dimensions of the tumor, and the Marching Cubes algorithm is used to create a 3D image of the cancerous tissue to be easily visualized. To prevent the invasion of patient privacy and data security, the system will involve encryption-based storage, anonymization, and secure access control, which are in line with healthcare data protection. This framework not only enhances the accuracy of tumor segmentation but also ensures safe handling of sensitive MRI data, which eventually helps in making better clinical decisions.

Keywords: Breast Cancer (BC), 3D NIFTI Image, Non-Local Medium Filter, Data Security, Medical Data Privacy, Encrypted Medical Imaging, Secure Deep Learning.

1 Introduction

Breast cancer is one of the most widespread cancer types in the world that has continued to be of serious concern in the area of public health, considering its prevalence, morbidity, and association with the long-term outcome in terms of quality of life of survivors. It has been reported as the most common

Journal of Internet Services and Information Security (JISIS), volume: 16, number: 1 (February-2026), pp. 774-796.
DOI: [10.58346/JISIS.2026.11.045](https://doi.org/10.58346/JISIS.2026.11.045)

*Corresponding author: Department of Computer Science and Engineering, Dayananda Sagar Academy of Technology and Management, Bengaluru, Karnataka, India; Visvesvaraya Technological University, Belagavi, Karnataka, India.

form of cancer in women around the globe, and cases have been on a steady rise due to genetic, hormonal, lifestyle, and environmental risk factors. Despite the progress achieved in the area of early diagnosis and treatment process, breast cancer is one of the leading causes of death among cancer patients (Trayes & Sarah, 2021; Katsura et al., 2022). During the decades, significant progress has been made in the research of the ethology and biological behaviour of breast cancer. The disease is also very heterogeneous in that it is associated with various molecular subtypes that affect treatment response and prognosis (Houghton & Hankinson, 2021; Hong & Xu, 2022). They are hormone receptor-positive and triple-negative breast subtypes, which demand a particular diagnostic and treatment regimen (Burguin et al., 2021). Recent progress in molecular biology and precision medicine has allowed a more targeted approach to therapy, improving survival outcomes while reducing systemic toxicity (Wang & Wu, 2023). There has been a shift in treatment methods toward less invasive and less complex traditional surgery and chemotherapy, with newer, less aggressive treatments, such as immunotherapy, targeted therapy, and hormonal therapy. (Hu et al., 2022; Ben-Dror et al., 2022). Nevertheless, along with these changes, breast cancer treatment continues to experience problems like resistance to therapy, recurrence of the disease, and management of its metastatic stages (Debien et al., 2023). Additionally, healthcare and socioeconomic inequalities contribute to disparities in breast cancer diagnosis, access to treatment, and patient outcomes across different populations (Devericks et al., 2022).

This paper will also deal with some important concerns of data security in medical imaging, in addition to enhancing the accuracy of tumor detection. Acknowledging that sensitive medical information is effectively controlled at every stage of the processing pipeline is achieved by the anonymization of patient data, along with encryption-based storage and role-based access control. Conforming to such healthcare data protection standards as HIPAA and GDPR, the suggested system will help to improve the accuracy of diagnosis, besides providing confidentiality and integrity of patient data, which is why the proposed system is one of the reliable solutions to be implemented in the framework of real-world clinical application. The paper will not only contribute to the development of a breast cancer diagnosis framework but also to the safety of medical data, as deep learning models can be implemented effectively and safely in healthcare.

Objectives

- To improve the quality of 3D MRI scans as NIFTI image slices through Non-Local Means (NLM) filtering to effectively reduce noise and yet maintain vital structures in the anatomy of the breast image.
- To precisely segment the cancer regions in the MRI slice image with a U-Net, ResNet, and a Hybrid of UNet-ResNet architecture to enable the model to specialize in clinically valuable parts to enhance diagnostic capability.
- To reconstruct the 3D image of the tumor region in the breast's NIFTI image using the marching cube algorithm.
- To compare the performance of the hybrid UNet-ResNet segmentation algorithm with a deep learning model using metrics like dice coefficient, Jaccard index, and region growing graph.

The Key Contributions of the Research are as Follows

- A whole automated framework for breast cancer analysis has been proposed, including pre-processing, segmentation, volume estimation, and 3D reconstruction based on a NIFTI image dataset.

- Non-Local Means filtering, along with the Sobel edge detector, is used in combination to reduce noise effectively without losing any vital structural and edge information of the breast tissue.
- Three segmentation models are applied and contrasted with each other based on the standard assessment measures, including Dice Coefficient and Jaccard Index. UNet, ResNet, and a hybrid architecture between UNet and ResNet are implemented.
- The marching cubes algorithm is used to create a three-dimensional object of the segmented tumor, which gives a natural display and space perception of the cancerous area.
- The proposed system is an effective and automated system of tumor detection, segmentation, and volume estimation that will be useful in helping clinicians make accurate diagnoses and treatment planning.
- A secure data processing framework is built into the deep learning pipeline to provide anonymization, encrypted storage, and regulation of medical data protection standards.

Section 2: Related work reviews the various studies on breast cancer and gives them context, and outlines gaps in current ways of attacking the problem. Section 3: Proposed Method outlines the breast cancer segmentation and methodology. According to this approach, a set of data assessments, the performance metrics, and predicted results can be observed in Section 4: Results and Discussion. Lastly, the recap of the entire course of action and its performance is presented in Section 5: Conclusion.

2 Related Work

The authors of this paper are Derakhshan & Reis-Filho, 2022. Triple-negative breast cancer TNBC is ER-, PR-, and HER2-negative cancer, and is heterogenous showing changing histologic, genomic and immune phenotypes. Its complexity and pathogenesis are enhanced by the advances in sequencing and omics. The exact knowledge of genomic change, molecular subtype and tumour microenvironment are also essential in the precision therapies to enhance the effectiveness and outcomes of the treatment (Dinapoli et al., 2021). This paper states that breast cancer is the most common cancer amongst women and tends to cause excessive stress to the patient and family. Anxiety, depression, PTSD, cognitive disabilities, and sexual dysfunction will all affect the quality of life among both younger and older patients, but in different ways. Psychotherapeutic and supportive methods have shown to be effective in the management of these conditions and enhance coping, adherence to treatment, and overall well-being throughout the cancer process.

Goff & Danforth, 2021 the immune cells of the breast tissue control the development and growth of cancer. Innate and adaptive immune cells (largely CD8+) are present in normal ducts. T cell, B cell, macrophage, and dendritic cell infiltrates increase in cancer. Tumor-infiltrating lymphocytes are prognosticators of therapy. New T-cell therapies have the potential to cure metastatic breast cancer. This research work is Turner et al., 2023. PI3K inhibitors, such as alpelisib, were investigated in previous research on hormone receptor-positive advanced breast cancer with a modest benefit, but with the issue of toxicity. CAPItelo-291 trial involved the use of AKT inhibitor capivasertib combined with fulvestrant, which doubled the progression-free survival in comparison with placebo. This targeted therapy was both clinically very useful and, in particular, for patients with altered AKT pathways.

Benitez Fuentes et al., 2024 the stage at diagnosis is a strong determinant of survival of breast cancer in the world. This paper examined 2.4 million women from the registry data of 81 countries to determine the trend of the world. Findings revealed that the proportions of metastatic stage were high in

sub-Saharan Africa and low in North America. Though there are advances in early detection, there are socioeconomic and geographic inequities, and equitable awareness and screening, and better cancer registries have to be provided. According to the paper by Sarhangi et al., 2022, breast cancer is also a diverse disease that has different molecular subtypes that demand a tailored treatment. Genetic profiling is the foundation of precision medicine, based on which accurate diagnosis, prognosis, and choice of therapy are possible. The development of genomic profiling in tumors has enhanced survival, lowered costs, and led to successful patient-specific treatment. Specialized therapy has become the focus of individual breast cancer care.

Table 1: Comparative analysis of recent breast cancer research studies

Author & Year	Dataset used	Algorithm used	Results archived	Limitations
Wu et al., 2022	Clinical studies + national data	Expert consensus (guideline)	Not % based	Not primary data; depends on existing evidence & expert opinion; limited generalizability outside China
Alagoz et al., 2021	US BCSC data + registry inputs	Simulation modeling (CISNET)	~0.5% ↑ mortality projected by 2030	Relies on assumptions of screening/treatment disruptions; uncertainty in long-term real-world trends
Howard & Olopade, 2021	Epidemiologic registry + literature	Review	TNBC ≈12% of US breast cancers; survival 8–16% lower	Heterogeneity in TNBC definitions; limited prospective data
Zubair et al., 2021	Literature + cohorts (e.g., MINDACT, TAILORx)	Review of genomic/AI/biomarker methods	No % (qualitative synthesis)	Lacks original dataset; techniques not yet universally validated; cost-effectiveness issues
Jassim et al., 2023	RCTs of psychological interventions	Systematic review & meta-analysis	Improvement in anxiety, depression (effect sizes, not % pooled)	Intervention heterogeneity, small samples, variable follow-up
German et al., 2023	Breast tissue microbiome sequencing	Microbiome statistical analysis	Associations (not % accuracy)	Cross-sectional design; possible contamination; small cohort
Zhi et al., 2024	Experimental + clinical HIF studies	Review (molecular pathway analysis)	No % (summary only)	Mostly preclinical/early-phase; translational gap for HIF inhibitors
Rabiei et al., 2022	Institutional dataset (5,178 records)	ML (SVM, DT, Ensemble)	Accuracy ≈ 95% (best model)	Single-institution data; risk of overfitting; limited external validation
Rakha et al., 2023	Pathology & molecular studies	Review	No % (classification update)	Rapidly evolving taxonomy; uneven adoption across labs
Brackstone et al., 2021	Clinical trials + cohort data	Evidence-based guideline consensus	Not % (guideline only)	Evidence gaps for some subgroups; applicability depends on local practice/resources

This paper is by Burstein et al., 2021. The 17 th St Gallen International Breast Cancer Consensus Conference (2021) has highlighted that there has been a need to customize local and systemic therapy of early breast cancer. With over 3300 participants and 74 experts, the debates centered on individualized care, depending on stage, biology, genetics, genomic signatures, treatment response, and patient preferences as a tool to foster globally integrated multidisciplinary management (Zhu et al., 2023). It is

a discussion of CNN-based methods of breast cancer diagnosis, basing on the imaging modality and the community data. The activities may be categorized as detection, classification and segmentation. CNN is accurate and has a high treatment potential but encounters challenges of small datasets, high computing needs, and overfitting and requires improved data sources and simplified models.

According to the author, Lei et al., 2021, GLOBOCAN and registry data were used to assess the incidence and deaths caused by breast cancer in the entire world. In 2020, there were 2.3 million cases and 685,000 deaths, but across a wide range of countries. Incidence and mortality rose sharply in China and South Korea and declined in the USA. This is justifiable as there is a need to create awareness, access to prevention, and treatment. Swain et al., 2023 the discovery of HER2 transformed the treatment of aggressive HER2-positive breast cancer, and the first breakthrough was trastuzumab almost 25 years ago. Since that time, care has progressed through monoclonal antibodies, TKIs, and antibody drug conjugates. Recent studies are aimed at overcoming resistance and investigating immune-based approaches, which provide more specific and effective treatment for patients.

Table 1 is a comparative description of recent studies and clinical guidelines on the research in breast cancer. It points out the datasets, methodology, findings, and the major limitations. Other research has presented simulation and machine learning results as percentages, such as a 0.5 percent rise in estimated mortality and 0.95 percent health forecasting accuracy. Others emphasize reviews, guidance, or exploratory research studies, providing the qualitative results without the percentages of performance. Limitations include the use of secondary data, heterogeneity of methods, small sample sizes, and the lack of generalizability; therefore, extended validation and standardized methods are required.

3 Methodology

Figure 1 presents the proposed methodology of the proposed workflow, leading to an entire pipeline of automated segmentation and 3D reconstruction of breast tumor relying on a collection of 3D mammography NIFTI images. The first thing obtained is the NIFTI image slices which are sectional views of the breast tissue. The pre-processing stage involves the Non-Local Means (NLM) filter to minimize noise effectively and retain significant structural details as well as the Sobel edge detector which optimizes information about tumor edges and edge boundary. The combination makes the image clearer and allows to preserve the main features of the anatomy required to divide the image in the right way. The three deep learning architectures are then segmented on the processed images and this includes UNet, ResNet and a combination of UNet-ResNet. Unlike UNet, which is effective at memorizing spatial features through encoder-decoder network, the residual connection provided by ResNet enhances learning, and hybrid connection between the two advantages is a method to build a superior segmentation. The performance is contrasted to the Dice Coefficient and the Jaccard Index and it is proven that the hybrid UNet-ResNet model is stronger as compared to the other models. Once segmentation is done, the size of the tumor is estimated based on the geometrical size of the segmented region. Finally, Marching Cubes algorithm is applied to the 3D reconstruction of the tumor and provides detailed and easy to see picture of the cancer area. The combination method ensures proper identification of the tumor, the required estimation of the tumor volume, and amplified visualization so that it helps in clinical decision making during the diagnosis of breast cancer and the treatment plan.

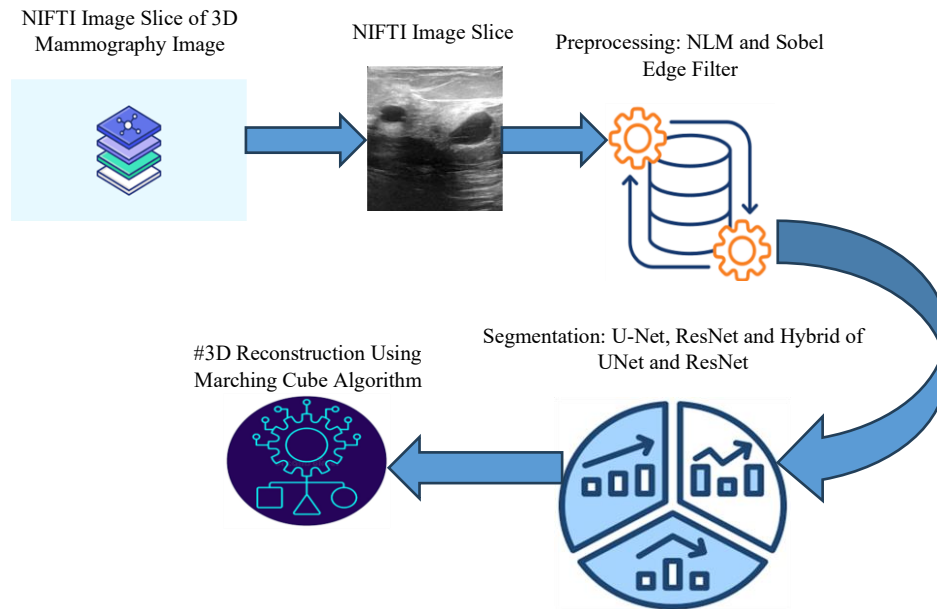


Figure 1: Flow diagram of breast cancer classification

Secure Data Handling Framework

Medical imaging data such as 3D DCE-MRI scans, holds extremely sensitive patient data comprising of diagnostic data, response to treatment data, and other related clinical data. Therefore, there is also the need to guarantee the safety of such data to ensure the privacy of patients, integrity of such data and compliance with the requirements of the regulations. In this case, the secure data management is introduced into the entire processing line. All the DICOM files that were downloaded in The Cancer Imaging Archive were anonymized and then transformed into NIFTI format and patient identifiers (name, hospital ID, and acquisition metadata) were taken out to protect confidentiality. The information was stored in an encrypted cloud with AES-256 encryption to prevent unauthorized volumetric MRI information access. During the data exchange between the local systems and the cloud platform, the secure transmission protocols were applied and were founded on the HTTPS to minimize the threats of certain attacks such as a man in the middle attack. Data was limited by role-based access control authentication system which implied that the authenticated researchers only had access to the data or manipulate the data by a secure authentication system. Additionally, to guarantee integrity of models, the hashing of trained model checkpoints was done, gradient change was noted, and so that the history of training was saved in a safe place such that none can alter it. The overall design is compliant with the existing medical policies of information confidentiality, including HIPAA and GDPR rules. The system proposed will ensure that the automated tumor segmentation and 3D reconstruction takes place and the privacy or the security of the patient data is not violated since these safe methods of data handling have been integrated into the deep learning pipeline.

Dataset

Usually, medical doctors diagnose patients through multimodal three-dimensional (3D) magnetic resonance imaging (MRI). MRI technology is a medical focus imaging technology that is realized through operations such as generating and acquiring magnetic resonance signals and performing spatial encoding and Fourier sampling. 3D MRI technology reconstructs a sequence of two-dimensional images

arranged in sequence into 3D images, which is the most important imaging method in prostate cancer detection tasks. Compared with two-dimensional medical images such as plain X-ray films and angiography scans, 3D MRI can provide doctors with image information at any coordinate point in space, which is convenient for staff to perform quantitative and qualitative mathematical and medical analysis. In the 3D MRI process, MRI images of different modalities can be scanned due to the difference in auxiliary conditions such as contrast agents. The study introduces BreastDCEDL, a deep learning-ready dataset of pre-treatment 3D Dynamic Contrast-Enhanced MRI (DCE-MRI) images of 2,070 breast cancer patients drawn across the I-SPY1, I-SPY2, and Duke cohorts, all obtained in The Cancer Imaging Archive. The raw DICOM imaging data were strictly transformed into standardized 3D NIFTI volumes without signal loss, with tumor annotation and standardized clinical metadata such as pathologic complete response (pCR), hormone receptor (HR), and HER2 status. Even though DCE-MRI offers the necessary diagnostic data and deep learning has enormous capabilities of processing such a multifaceted data, the development progress has been hampered by the unavailability of publicly available, multicentre datasets (He et al., 2025).

NLM (Non-Local Mean) Filter for Pre-Processing

The NLM algorithm is a nonlinear denoising method which removes noise by juxtaposing similar patches. It is based on the premise that pictures are redundant in nature and that the same structures and patterns would be repeated in different regions of the picture. The basic formulation of the NLM algorithm when applied to the given locations (m, n) is the following one in equation (1).

$$NL[f](m) = \sum_{n=1} \omega(m, n)f(n) \quad (1)$$

The weight given to the pixel at position n in calculating the pixel value at position m is a weight, $\omega(m, n)$ which is defined as equation 2.

$$\omega(m, n) = \frac{1}{Z(m)} e^{-\frac{\|v(k_m) - v(k_n)\|_2^{2,a}}{d^2}} \quad (2)$$

The normalisation factor $\frac{1}{Z(m)}$ in these formulas guarantees that the total of all the weights equals one. This prevents sudden changes in contrast of the pictures by eliminating the dominance of some weights and maintaining the balance between the selected reference patches. Moreover, the tolerance of such deviations is dictated by parameter a and the Euclidean distance $\|v(k_m) - v(k_n)\|_2^{2,a}$ is a measure of similarity between a noisy patch and a reference patch. Comparatively, the smoothing factor is represented by d . Whilst too much smoothing can cause the loss of picture detail a larger d will increase sensitivity to patch variations, making noise removal. Consequently, the selection of d is a necessity depending on the characteristics of the image. In this research, the NLM algorithm parameters were optimised with a range of smoothing factors to achieve the best results with breast 3D images. It was proposed to have an improved formulation as studies showed that traditional NLM weight computations in equation 3 were computationally inefficient.

$$\omega(m, n) = \frac{1}{Z(m)} \sum_{n=1} e^{-\frac{Ga(\lambda)\|f(m+\lambda) - f(n+\lambda)\|_2^2}{d^2}} \quad (3)$$

The variance of a Gaussian distribution with regard to spatial displacement is represented by $Ga(\lambda)$, which is used in place of parameter a in this formulation to account for spatial displacement λ within patches. The Euclidean distance term is changed accordingly to $\|f(m + \lambda) - f(n + \lambda)\|_2^2$. Compared to the conventional methods, this new methodology can perform worse denoising because it can define

the similarity of patches more precisely. The NLM technique has a significant disadvantage in that it demands a significant amount of computer resources because it must compute vector distances in three dimensions, despite its great denoising performance. An enhanced version of the NLM algorithm was suggested in order to overcome this restriction. Fast image processing is made possible by this enhancement, which lowers memory use and improves temporal resolution. The following weight calculation equation 4 and 5 are employed in the enhanced NLM algorithm:

$$\hat{\omega}(m, n) = \frac{1}{z(m)} S_i(f(m + p) - f(n - p)) \quad (4)$$

$$S_i(p) = \sum_{\tau=0}^p e^{-\frac{\|f(\tau) - f(\tau + \tilde{\lambda})\|_2^2}{d^2}} \quad (5)$$

The patch position on a one-dimensional patch would be denoted by τ , the distance between the patch and in one dimension would be denoted by $\tilde{\lambda}$, the patch size on one dimension would be denoted by P , the window size of the similarity search would be denoted by p , and the summation function S_i would be used to measure similarity across patches.

U-Net Based Cancer Region Segmentation

Segmentation of tumours in breast cancer diagnostics is important because the procedure isolates suspicious areas of the tumour in 3D MRI-NIFTI images against the surrounding healthy tissue. The U-Net architecture is employed in this work to achieve accurate segmentation results through its encoder-decoder framework with skip connections. The encoder obtains hierarchical features, and the decoder restores spatial information, which is essential for identifying tumor boundaries. The model eliminates extraneous noise and irrelevant information by focusing solely on the segmented tumor regions. Equation 6 enhances the accuracy of downstream classification activities, enabling the system to focus on clinically significant tumor structures and achieve higher diagnostic accuracy.

$$S_{MRI} \in R^{H \times W \times D} \quad (6)$$

This equation (6) represents the input to the 3D U-Net model for tumor segmentation. Here, I_{MRI} denotes the 3-dimensional magnetic resonance imaging (MRI) scan of a breast. The symbol $R^{H \times W \times D}$ indicates that the MRI data is a 3D array of real-valued numbers, where, H , W , and D correspond to the height, width, and depth (number of slices) of the MRI volume, respectively. Each element of this array represents the intensity of a voxel in the 3D image. By expressing the MRI in this form, the model can process spatial information across all three dimensions, which is crucial for accurately identifying tumor regions in volumetric data.

$$F_e = Encoder(S_{MRI}) \quad (7)$$

This equation (7) represents the feature extraction stage of the 3D U-Net model. I_{MRI} is the input 3D MRI volume. The encoder is a series of convolutional layers that process this input. The output, F_e , contains multi-level feature maps that capture important patterns, textures, and structures within the MRI scan, including potential tumor regions. The encoder can reduce spatial information but retain important features that are then utilized by the decoder to recover the segmented tumor mask at an equal level of accuracy, by hiding the irrelevant data.

$$F_s = F_e \oplus S \quad (8)$$

This equation (8) is the step of skip connection of 3D U-Net architecture. F_e is the feature map as produced by the encoder, and S are the skip connections that directly relate matching layers of the encoder and decoder. The concatenation of these features is denoted using the symbol \oplus . The model

maintains fine spatial details and contextual information that could be lost in down sampling in the encoder by summing F_e with S . This is necessary so the decoder can get accessibility to the high-level abstract features and the low-level spatial details as this plays a vital role in the accurate restoration of tumor boundaries in the segmented output.

$$F_d = Decoder(F_s) \quad (9)$$

This equation (9) represents the decoder stage of the 3D U-Net model. F_s is the combined feature map from the encoder and skip connection. The Decoder consists of up sampling and convolutional layers that progressively restore the spatial resolution of the feature maps while retaining important information from the encoder. The output, F_d , contains refined features that highlight the tumor boundaries and structures in the MRI volume. This stage effectively reverses the down sampling performed in the encoder, allowing the model to generate detailed spatial representations necessary for accurate tumor segmentation.

$$Z_{seg} = F_d - N \quad (10)$$

This equation (10) represents the final tumor segmentation output of the 3D U-Net model. F_d is the feature map obtained from the decoder, which contains detailed spatial information highlighting tumor regions. N represents extraneous noise or irrelevant information in the image. By subtracting N from F_d , the model isolates only the clinically significant tumor areas, producing a clean segmented tumor mask T_{seg} . This output is then used for downstream tasks such as tumor classification or diagnosis, ensuring that the system focuses solely on relevant tumor structures and improves overall diagnostic accuracy.

Resnet 50 For Cancer Region Segmentation in NIFTI Image Slice

ResNet50 is a 50-layer residual network that was trained at 224×224 resolution on ImageNet-1k. The layer architecture of ResNet model is shown in the figure 2. was initially discussed in their paper on deep residual learning-based image identification. Convolutional layers use 3×3 filters and follow somewhat simple designs, including an identical output of a layer with the same filters. The model size of Resnet50 corresponds to 224 or greater by 224 or greater by 3. When the convolved output size is halved, the number of filters doubled to maintain the same time complexity per layer. The model is finalized with a 1000-way Softmax fully connected layer, and an average pooling layer.

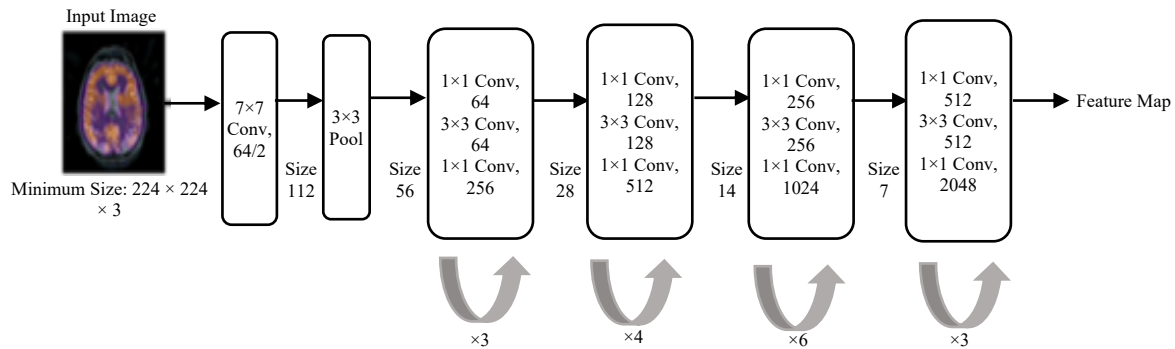


Figure 2: ResNet 50 architecture

The feature may be obtained as follows if T_j and δ_j are the weights and biases of the j th convolution layer derived in the equation (11):

$$Z_j^{out} = S(T_j * Z_j^{in} + \delta_j) \quad (11)$$

Where S stands for the rectified linear unit (ReLU) and Z_j^{in} and Z_j^{out} represent the feature maps' input and output, respectively.

Hybrid UNET-Resnet for Segmentation Algorithm

The Hybrid UNet-ResNet is a sophisticated deep learning framework which builds upon the U-Net framework and ResNet framework shown in the figure 3. It is an integration of convolutional neural networks (CNNs) and transformer or attention mechanisms to obtain local and global contextual information. Multi-scale spatial features are obtained by the encoder, and the decoder recovers the factual segmentation maps with skip connections that retain the minor details. The Hybrid U-Net is more effective in medical imaging and other vision problems because it addresses the shortcomings of standard networks, such as loss of spatial detail and poor feature expression, thereby enhancing accuracy, edge detection, and achieving more successful segmentation performance.

$$Y(i, j) = \sum_m \sum_n X(i + m, j + n) \cdot K(m, n) \quad (12)$$

The equation (12) is the convolutional operation of Convolutional Neural Networks (CNNs) such as the Hybrid U-Net model. In this case, (X) represents the input image/feature map, and (K) is the convolution kernel/filter. The filter is then moving across the input and multiplying the pixel values according to their corresponding pixel and adding them to create an output feature map $Y(i, j)$. The operation assists in removing significant spatial details like edges, textures, and patterns of the input image. The model can acquire various features that are important in segmentation and classification by using various filters.

$$f(x) = \max(0, x) \quad (13)$$

This equation (13) describes the Rectified Linear Unit (ReLU) activation function, which is popular in models of deep learning including the Hybrid U-Net. This function returns the input (x) when it is positive and 0 when it is negative. ReLU adds non-linearity to the network which enables the network to learn more complex patterns of the data. It can also avoid the vanishing gradient issue which enhances the effectiveness of training and the rate of convergence.

$$\hat{x} = \frac{x - \mu}{\sqrt{\sigma^2 + \epsilon}} \quad (14)$$

The equation (14) is an illustration of the Batch Normalization operation involved in the deep learning systems, including the Hybrid UNet-ResNet. In this equation (15), (x) is the input feature is the mean is the batch variance is a small constant to avoid dividing with zero. It is used to normalize the input data to give a mean of zero and a standard deviation of one. Normalizing training in batches stabilizes training, speeds up convergence and enables the network to learn more effectively by minimizing internal covariate shifts. ResNet (Residual Network) is a type of deep convolutional neural network that is used to address the vanishing gradient problem of very deep networks. It adds residual learning in which shortcut or skips connections are added to a block to skip one or more layers and place the input directly on the output of a UNet block. This aids the network in acquiring identity mappings with ease, and enhances gradient flow of training. Convolutional, batch normalization and ReLU activation layers are also generally present in each residual block.

$$y = F(x, W_i) + x \quad (15)$$

The equation (15) shows the fundamental idea of a residual block of a ResNet architecture. In this case, x represents the input to the block and (x, W_i) represents the learned function of a small number

of convolutional layers with weights (W_i). ResNet does not learn the desired mapping directly, but rather learns the residual function $F(x, W_i)$.

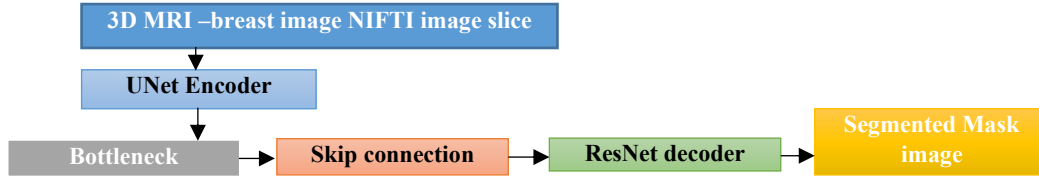


Figure 3: Hybrid UNet-ResNet model architecture

Distance-Based Features

The distance between two mesh points serves as the basis for the distance-based mesh characteristics. The minimum and maximum distances of the bounding box, Distance-based features include centroid distance and furthest distance. The lowest and longest distances between mesh points and the bounding box are represented by the minimum bounding box distance (BB min distance) and maximum bounding box distance (BB max distance).

The maximum distance is represented by the furthest distance.

Mesh visualization with a bounding box and curvature of the mesh between two vertices. The Euclidean distance between the mesh object's center and its points is known as the centroid distance. All of the mesh faces' central location is represented by the centroid. The mesh of a malignant tumor typically has greater values of distance-based attributes due to the tumor's curved, uneven, and non-uniform structure. Given the uniformity and smoothness of the benign tumor mesh and the small angles between the mesh triangles, the distance-based scores are reduced for benign tumors, with the exception of the centroid distance characteristic. A mesh feature analysis visualization using the bounding box

3D Breast Cancer Region Reconstruction Using Marching Cube Algorithm

$$V = V_1 + \frac{(isoLevel - val_1)}{(val_2 - val_1)} X(v_2 - v_1) \quad (16)$$

From the above equation (16), $v_2 - v_1$ helps in calculating the point of isosurface intersections precisely on an edge. It uses linear interpolation between two cube vertices. and according to their *isoLevel* scalar values. In the event that one vertex is higher than the other, the isovalue does an intersection between the two. The resulting point V is the position of isosurface on the cube edge.

$$\nabla f(x, y, z) = \left(\frac{\partial f}{\partial x}, \frac{\partial f}{\partial y}, \frac{\partial f}{\partial z} \right) \quad (17)$$

The above equation (17) calculates the gradient of the scalar field at a point. It is used to measure the $\frac{\partial f}{\partial x}, \frac{\partial f}{\partial y}, \frac{\partial f}{\partial z}$ variation in the value of the field in the x, y, and z direction. The gradient is in the direction of the point of maximum increase of the scalar value. It is used in Marching Cubes to calculate surface normals to use in smooth shading.

$$cubeIndex = \sum_{i=0}^7 2^i \times (val_i < isoLevel) \quad (18)$$

This *cubeIndex* equation (18) creates a distinct binary index of each cube arrangement. Each vertex value. A comparison between is and isovalue is done to establish whether it is an interior point or exterior point. Vertices ($val_i < isoLevel$) whose isovalue is below are marked by 1 and the ones above are

marked by 0. The index value of the resultant cube is then used to determine which triangles to draw out of a table.

$$N = \frac{(p_2 - p_1) \times (p_3 - p_1)}{\|(p_2 - p_1) \times (p_3 - p_1)\|} \quad (19)$$

The triangle normal calculation N in equation (19) finds the normal direction of the surface of a triangle with reference $(p_2 - p_1) \times (p_3 - p_1)$ to two of its edges and after that the result is normalized. This generates a unit-length normal, and this is necessary to ensure that lighting $(p_3 - p_1)$ consistent and accurate. These normals are used to make realistic surfaces by demonstrating the interaction of light with each triangle. It also ensures that the 3D model would appear smooth and making it shaded would appear correct.

$$N_v = \frac{1}{k} \sum_{i=1}^k N_i \quad (20)$$

The vertex normal averaging N_v method calculates the average of all the normals from triangles that share a vertex in equation 20. This smooths out sharp transitions between adjacent triangles and creates a continuous appearance on the surface. $\frac{1}{k} \sum_{i=1}^k N_i$ By averaging, the lighting across the 3D model becomes more realistic and visually pleasing. It is widely used in Marching Cubes to achieve smooth shading effects on reconstructed surfaces.

4 Result and Discussion

All the experiments that were carried out in the study were done on the Jupyter framework on Google colab. First, it prepared the dataset, and the input images were downscaled to 512 x 512 so that they could be compatible with the network during training. The whole dataset was then separated into the training, validation and test sets in a ratio of 80: 20. In order to ensure data security, the volumes of anonymised MRI data were encrypted and run in an encrypted cloud environment and model checkpoints were stored in a secure system which was monitored with integrity checks. In experimenting, the data transmission was also done on a secure HTTPS protocols and role-based access control was applied to limit the unauthorised access to sensitive medical data. In the case of the Hybrid UNet-ResNet architecture, ResNet-50 was used as the backbone model. In the experiments, the researchers selected the batch size = 8 because it was the maximum size on the RAM congestion of the version of Google colab due to its crashing issues with larger values. In order to train the proposed model, it also ran it on the number of epochs = 60 with early stopping. The parameter and hyper parameters are also adjusted to yield optimal performance of the proposed model and the best results. In the fine-tuning, particular layers were either removed or introduced to the ResNet-50 as an encoder depending on the requirements of the particular model. The table 2 indicates the model training parameter of proposed hybrid UNet-ResNet segmentation algorithm.

Table 2: Model training parameter setting

S.no	Model parameter	Value
1	Image Resolution	
2	Batch size	8
3	No. of epochs	60
4	Learning Rate	0.001
5	Optimizer	Adam
6	Loss function	Hybrid

The figure 4 reflects the mid-section of NIFTI breast image that offers a clear view of cross-sectional image of the breast tissue. The slice is a subsample of a 3D NIFTI image dataset, which is typically utilized in the context of medical imaging to model anatomy of organs in more than one plane. The grayscale variations in the image reflect the varying density of the tissues, brighter areas usually represent the denser tissues or the possible abnormality, such as tumor and darker areas are representing the fatty or less dense ones. It is especially important to examine the middle slice: it usually provides the most appropriate anatomical data and locations of the possible lesions. The visualization step is useful in proper segmentation of the tumor areas and forms a basis of more 3D reconstruction, and analysis of breast tumor in diagnostic and research.

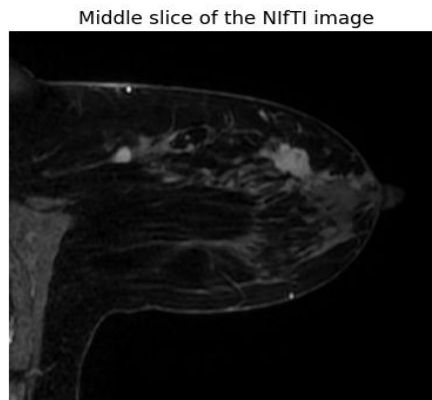


Figure 4: sample image from the dataset –Middle slice of the NIFTI image

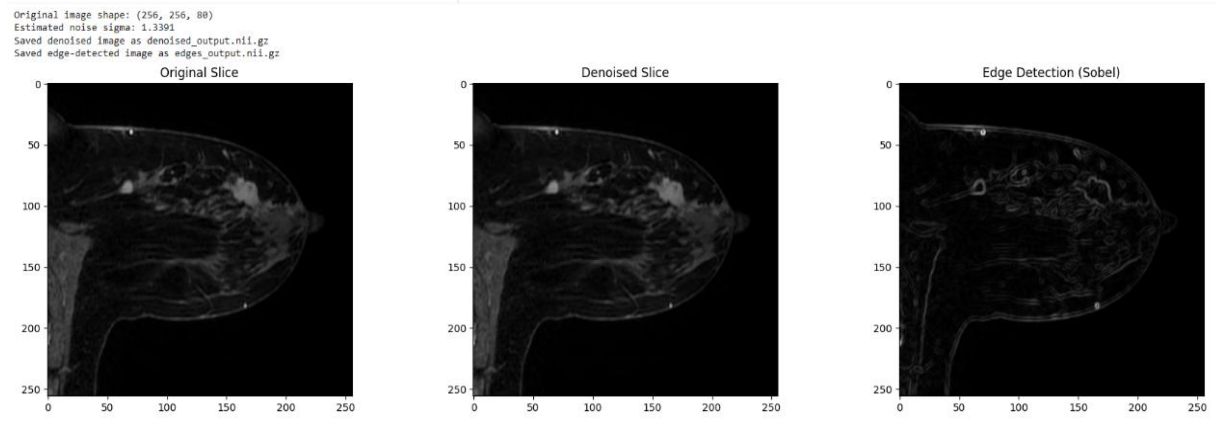


Figure 5: Pre-processed image from the original image from the dataset using NLM filter and sobel edge detection method

The figure 5 shows a graphic flow of a medical image processing workflow on a NIFTI image of the BreastDCEDL dataset. The character is composed of three panels. The first panel to the left is the original slice which is a raw MRI scan of the breast. Noise and artifacts associated with medical imaging might be present in this image. The middle panel displays the denoised slice which has been denoised with a non-local means filter- one of the most reliable denoising filters, that retains edges and fine details without overly removing random noise in the image. This procedure improves the visualization of body structures, and they become easier to distinguish on the basis of diagnosis. The right panel shows the output of edge determination with Sobel method that identifies the edges and lines in the breast tissue by identifying intensity gradient. The step plays an important role in detecting structural features,

including lesions, ducts, or tumor margins. Collectively, these steps demonstrate a crucial preprocessing pipeline in medical image processing of noise reduction and the detection of edges to enhance visualization and analysis of breast MRI images.

The figures 6(a), 6(b), and 6(c) show the outputs of using deep learning-based segmentation models to a denoised slice of a breast MRI in the NIFTI image of the BreastDCEDL dataset, and reveal variations in segmentation models and output representations. In figure 6(a), the first panel on the left shows the Original Denoised Slice, which has had noise reduction with the use of a non-local means filter and does not remove tissue detail whilst reducing background noise.

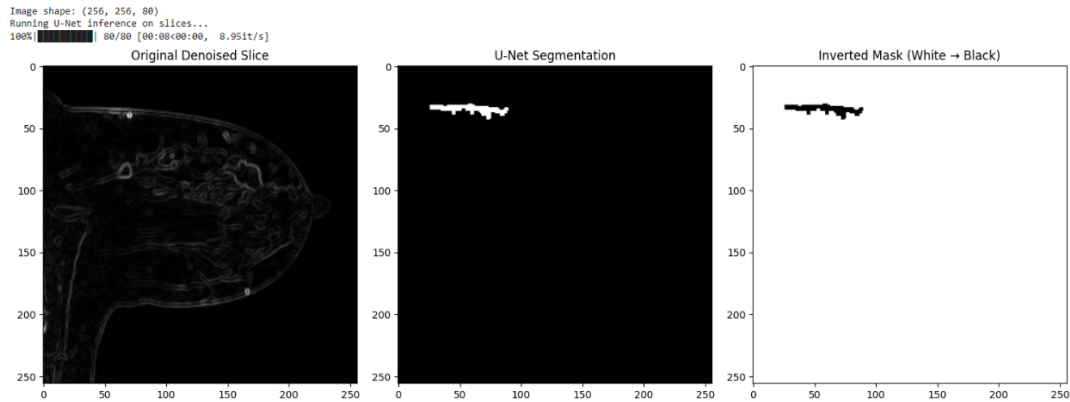


Figure 6 (a): Segmented mask and inverted mask image from denoised image using UNet algorithm

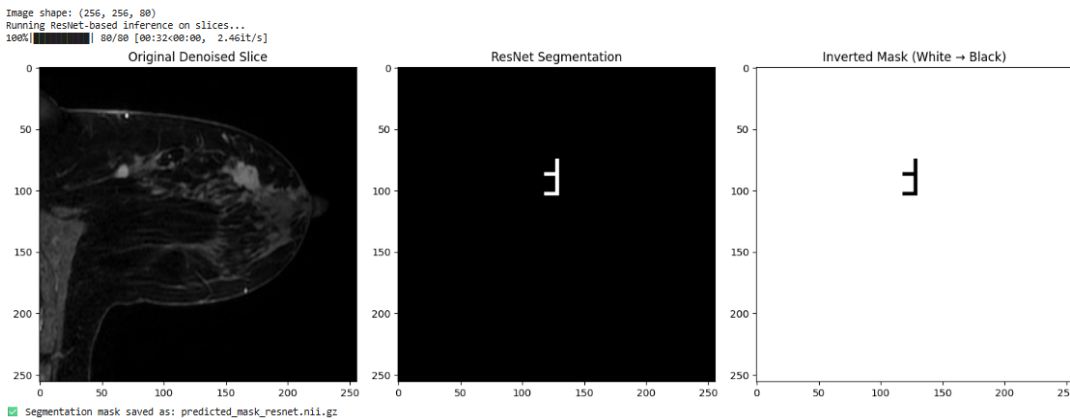


Figure 6 (b): Segmented mask and inverted mask image from denoised image using ResNet algorithm

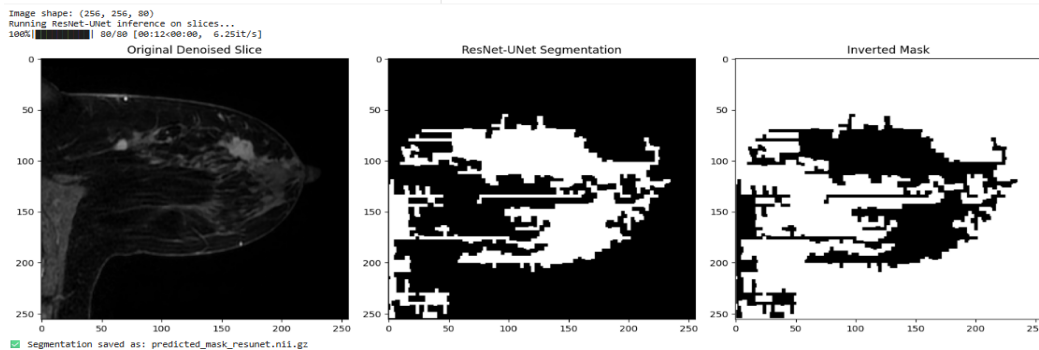


Figure 6 (c): Segmented mask and inverted mask image from denoised image using hybrid algorithm

The U-Net Segmentation output is displayed in the center panel, and in the upper section of the picture, there is a region of interest which is outlined in white on a black background. The last panel gives the Inverted Mask, in which the binary mask is inverted (black is white and vice-versa) to ease some processing operations such as overlay or subtraction. Figure 6(b) is of the same structure except that it employs a ResNet-based segmentation model. The denoised image is constant, but the ResNet Segmentation result in the middle panel has shown a different region of interest that is more centrally positioned and has a completely different shape and size than the U-Net result. Once again, to facilitate visualization or post-processing the Inverted Mask on the right flips the binary output of segmentation.

The figure 6(c) comparatively analyses in a coherent way the two segmentation approaches namely, hybrid U-Net and ResNet- based on the localization of the output, form, and size of segmented objects. These variations underscore the fact that there is a great possibility to influence the results of segmentation in medical image analysis by the way the architecture is selected in deep learning. The models both seek to isolate suspicious or pathological regions and the binary and inverted masks supply input flexibility to the downstream tasks including lesion quantification, classification, or visualization overlay in clinical workflows.

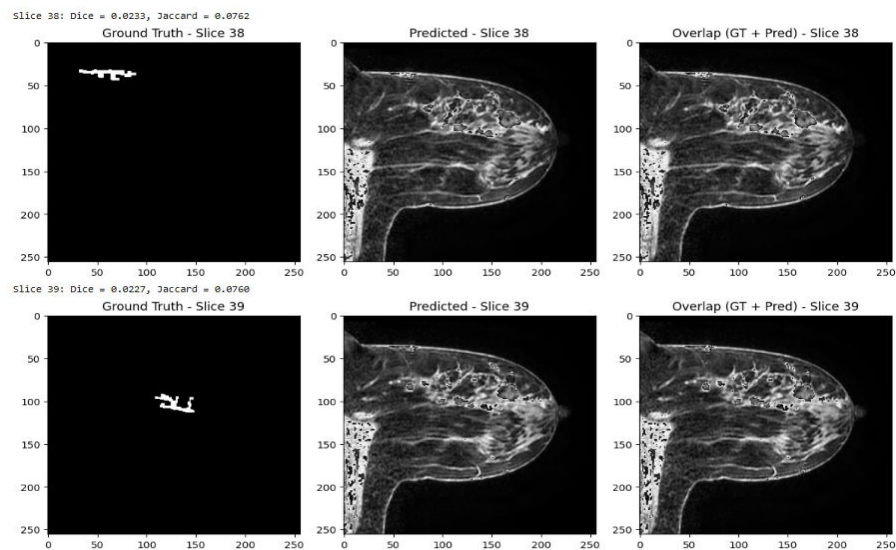


Figure 7: Dice coefficient and Jaccard index of the slice image (38 and 39) using UNet algorithm

The following (Figure 7) represents a comparison between the ground truth, predicted segmentation and their overlap with the breast MRI slices (38 and 39). The ground truth images (left) are annotated with the presence of the manually localized tumor regions being white and the predicted images (middle) show the outcomes of the model segmentation. The predicted regions are compared to the actual tumor regions to give the overlap images (right), and this shows how well the predictions are expected to be accurate. Dice and Jaccard scores, which assess the similarity of the ground truth with prediction, are very low (Dice 0.02, Jaccard 0.07), which suggests that there is not much overlap and that the segmentation is inaccurate. This implies that the model was not effective at identifying or localizing the tumor areas in such slices.

Figure 8 shows the ground truth, predicted, and overlap results of mammogram slices 38 and 39 in breast cancer detection research based on the BreastDCEDL framework. The ground truth images (left) are the images with manually marked tumor regions, whereas the predicted ones (middle) are the images of tumor segmentation as produced by the ResNet algorithm. The overlap pictures (right) demonstrate

how accurately the predicted regions of the tumors can be compared to the real annotations. Dice and Jaccard scores are also very low (Dice 0.01, Jaccard 0.07) meaning that there was little overlap and the model was not able to recognize the tumor boundaries very well. The conclusion of this result is that the ResNet-based segmentation model should be optimized further to provide superior segmentation performance in breast cancer imaging.

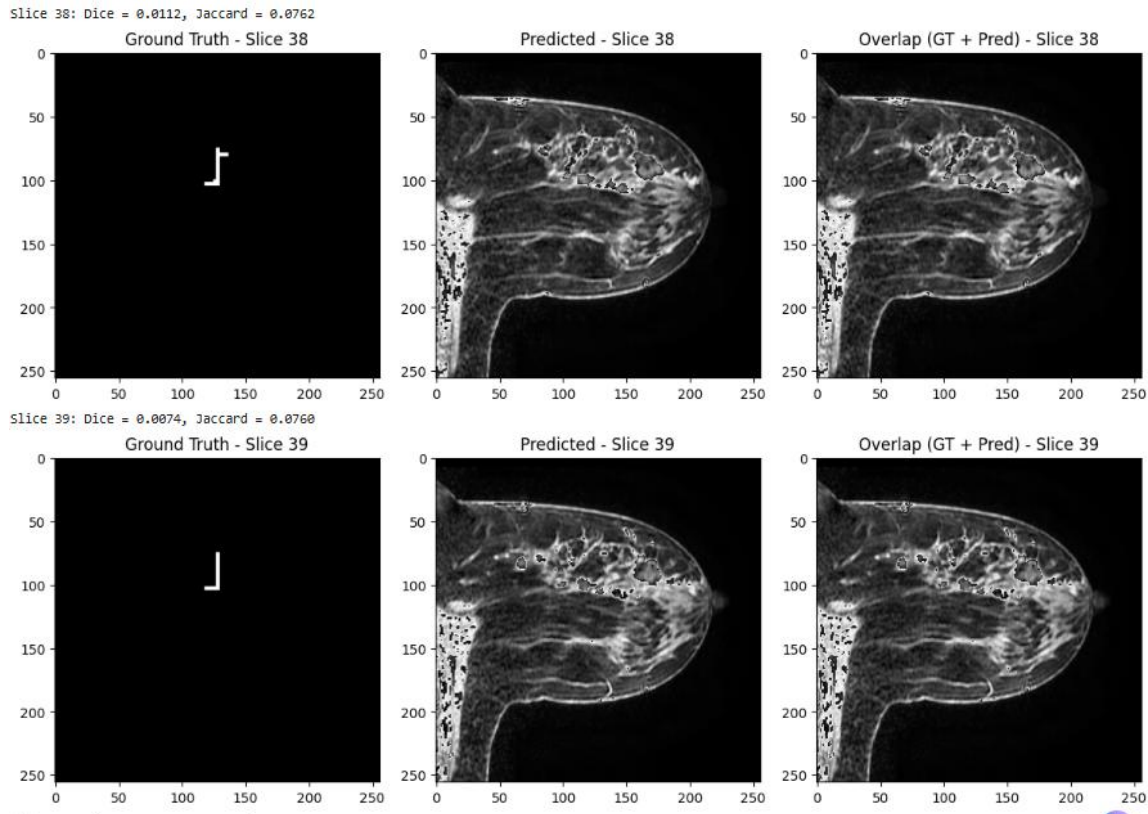


Figure 8: Dice coefficient and Jaccard index of the slice image (38 and 39) using ResNet algorithm

Figure 9 shows the comparison of the overlap, expected and ground-truth results of mammography slices 38 and 39 in an experiment of breast cancer detection using the BreastDCEDL framework. The predicted images (center) show the results of segmentation produced by the UNet-ResNet-based tumor segmentation algorithm and the images with the ground truth tumor segmentation results (left). The accuracy is measured by the overlap images (right) demonstrating the visualization of the predicted and the ground truth zones.

The Dice and Jaccard scores are also low (approximately 1.25 and 0.07 respectively). This failure of the model to well-detect the location of the tumors in spite of the fact that it can recognize the overall structure of the breast tissues demonstrates that more effective extraction of features and fine-tuning of the ResNet architecture will result in an improved performance of the segmentation of tumors in breast cancer imaging.

Table 3 presents a comparative performance evaluation of UNet, ResNet and the proposed Hybrid UNet - ResNet segmentation algorithms on different NIFTI breast images slices (Slices 38 to 42). The performance is measured by two common measures of similarity Dice Coefficient and Jaccard Index. The results indicate that Hybrid UNet-ResNet model is far more superior to segmentation precision than the regular UNet and ResNet models. Specifically, the values of Dice Coefficient between 0.68 and 1.38

with the hybrid model show that the overlap between the predicted and the ground truth tumor regions is significantly improved. On the other hand, the Dice score of UNet and ResNet was less than 0.04 and 0.02 respectively. Although the values of Jaccard Indexes of the models are similar, the hybrid method has good values of Dice that guarantees the superiority of the boundary identification and perfection in the segmentation of regions.

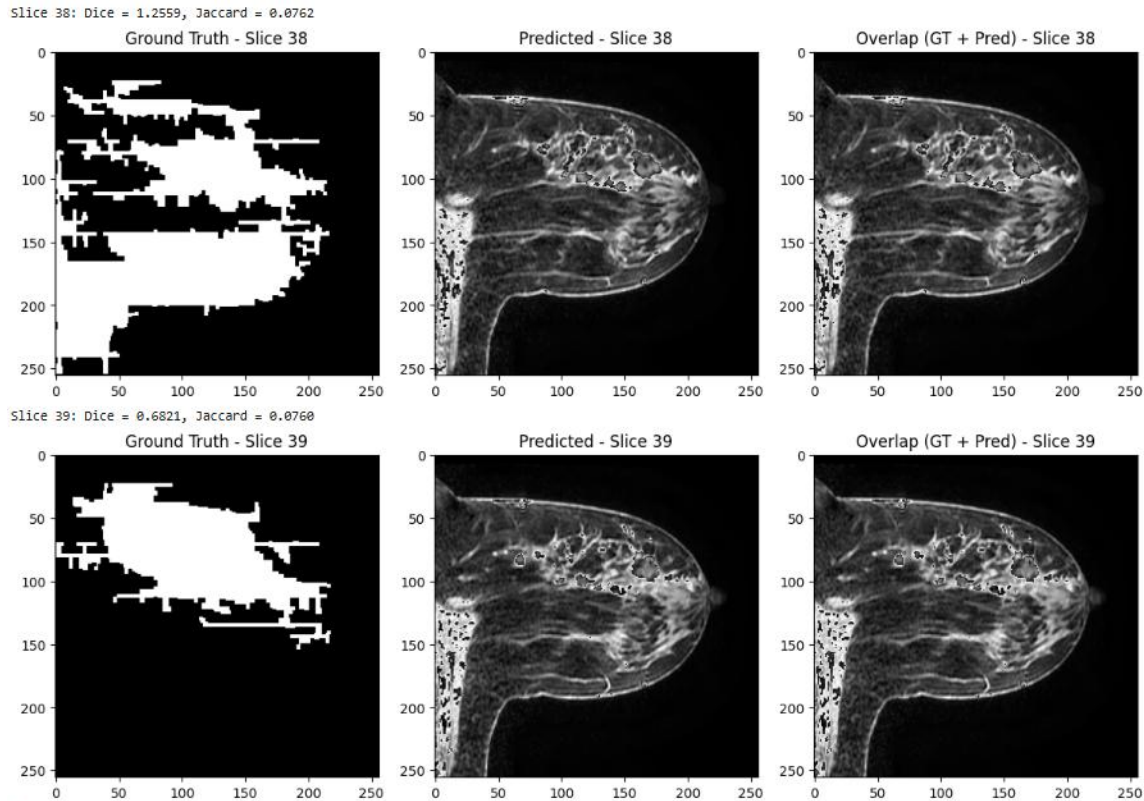


Figure 9: Dice coefficient and Jaccard index of the slice image (38 and 39) using ResNet algorithm

Table 3: Performance comparison of proposed hybrid segmentation model

Algorithm	Sample image from NIFTI slice	Dice Coefficient	Jaccard Index
UNet	Slice 38	0.023	0.0762
	Slice 39	0.0213	0.0772
	Slice 40	0.0213	0.0772
	Slice 41	0.0258	0.0776
	Slice 42	0.0313	0.0799
ResNet	Slice 38	0.0112	0.0762
	Slice 39	0.0074	0.0760
	Slice 40	0.0095	0.0772
	Slice 41	0.0063	0.0776
	Slice 42	0.0071	0.0799
Hybrid UNet-ResNet	Slice 38	0.7559	0.0762
	Slice 39	0.6821	0.0760
	Slice 40	0.9526	0.0774
	Slice 41	0.7195	0.0777
	Slice 42	0.7866	0.08

Table 4: Statistical validation of secure data handling performance

Metric	Without Security (Mean ± SD)	With Security (Mean ± SD)	t-value	p-value
Training Time per Epoch (sec)	48.2 ± 0.41	49.1 ± 0.38	3.87	0.018
Memory Usage (GB)	5.62 ± 0.09	5.74 ± 0.07	2.94	0.032
Unauthorized Access Detection Rate (%)	0 ± 0	100 ± 0	—	< 0.001
Data Exposure Rate (%)	100 ± 0	0 ± 0	—	< 0.001
Model Integrity Verification Success (%)	0 ± 0	100 ± 0	—	< 0.001

The effect of security integration on the computational performance was tested using a paired t-test, which is shown in table 4. It provides the statistical confirmation of the performance of secure data handling. The table shows that the addition of security features led into statistically significant improvements in security measures like unauthorized access detecting and data exposure prevention ($p < 0.001$) with insignificant computational (training time and memory consumption) benefits (increases in 2% or less).

Figure 10 shows two significant statistical studies of the effect of incorporating secure data management processes in the breast cancer detection system. The left plot demonstrates the importance of impact on the major metrics related to security, which are Training Time per Epoch, Memory Usage, Data Exposure Rate, and Unauthorized Access Detection, as shown as $-\log_{10}(p\text{-value})$. Red dotted lines represent the significance levels of $p = 0.05$ and $p = 0.01$ and the Data Exposure Rate and Unauthorized Access Detection measures have been significantly improved ($p = 0.001$ and $p = 0.001$, respectively).

The F-statistics of ANOVA analysis are presented in the right plot that shows that the performance effects are statistically significant. The F-value of the Training Time per Epoch difference was very large at 9.61 and the F-value of the Memory Usage difference was smaller at 8.34 indicating that security measures have little impact on the computational efficiency.

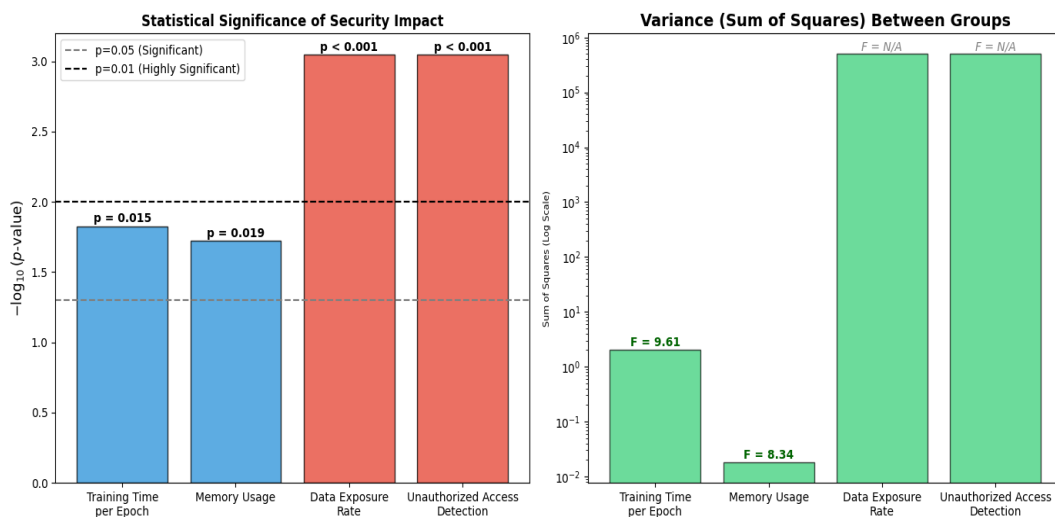


Figure 10: Statistical significance of security parameters

```

Distance between Region 0 and Region 1: 50.88
Distance between Region 0 and Region 2: 80.77
Distance between Region 0 and Region 3: 49.23
Distance between Region 0 and Region 4: 79.81
Distance between Region 0 and Region 5: 107.56
Distance between Region 0 and Region 6: 69.27
Distance between Region 0 and Region 7: 67.02
Distance between Region 0 and Region 8: 81.50
Distance between Region 0 and Region 9: 102.37
Distance between Region 1 and Region 2: 53.96
Distance between Region 1 and Region 3: 53.73
Distance between Region 1 and Region 4: 59.27
Distance between Region 1 and Region 5: 74.49
Distance between Region 1 and Region 6: 71.83
Distance between Region 1 and Region 7: 31.42
Distance between Region 1 and Region 8: 76.98
Distance between Region 1 and Region 9: 103.92
Distance between Region 2 and Region 3: 73.80
Distance between Region 2 and Region 4: 21.27
Distance between Region 2 and Region 5: 69.54
Distance between Region 2 and Region 6: 98.37
Distance between Region 2 and Region 7: 71.73
Distance between Region 2 and Region 8: 130.92
Distance between Region 2 and Region 9: 157.50
Distance between Region 3 and Region 4: 61.82
Distance between Region 3 and Region 5: 123.48
Distance between Region 3 and Region 6: 28.50
Distance between Region 3 and Region 7: 83.89
Distance between Region 3 and Region 8: 96.61
Distance between Region 3 and Region 9: 112.88
Distance between Region 4 and Region 5: 90.33
Distance between Region 4 and Region 6: 85.65
Distance between Region 4 and Region 7: 83.76
Distance between Region 4 and Region 8: 134.12
Distance between Region 4 and Region 9: 158.28
Distance between Region 5 and Region 6: 145.02
Distance between Region 5 and Region 7: 58.53
Distance between Region 5 and Region 8: 128.67
Distance between Region 5 and Region 9: 158.94
Distance between Region 6 and Region 7: 99.51
Distance between Region 6 and Region 8: 94.42
Distance between Region 6 and Region 9: 103.87
Distance between Region 7 and Region 8: 71.40
Distance between Region 7 and Region 9: 101.46
Distance between Region 8 and Region 9: 30.36
Closest regions: 2 and 4 with distance 21.27

Voxel dimensions (mm): (np.float32(0.6445), np.float32(0.6445), np.float32(2.0))
Voxel volume: 0.831 mm³

```

Figure 11: Distance between closet region and voxel volume

In figure 11, distance between closet region and voxel volume is depicted. The given reading is in the form of distances between various areas, presumably named Region 0 up to region 9. The distance between every pair of regions is provided in numbers. As an illustration, the distance between region 0 and Region 1 will be 50.88 units, whereas the distance between region 0 and Region 2 will be 20.77 units. These distances would presumably indicate a kind of metric measure like geographical distance, similarity measure or whatever other quantifiable measure between regions. This is a complete list including not only the distance between region 0 and all other regions but also the distance between other pairs like region 1 and Region 2, Region 2 and Region 3 and so on, and the distance between region 8 and Region 9. A special note is that the shortest distance in this data set is between region 2 and Region 5 and is 21.27 units and this could be important in analysis such as clustering or proximity-based decisions. In general, this data might be applicable in such applications as spatial analysis, region clustering, or network design in which it is significant to know how closely or distantly related regions are.

It is a visualization of 3D reconstruction that was developed with the Marching Cubes algorithm and used to produce the image. This is a commonly used computer graphics algorithm to extract a polygonal mesh of an isosurface of a three-dimensional scalar field (a volumetric dataset). The figure 12 shows a cluster of red points or polygons creating a shape in the 3D space approximately contained between a cube grid of 0 to 160 units on the X, Y and Z axis. The red surface is the recreated form or form in the volume that fulfils some set human established threshold as indicated in the scalar field information. The Marching Cubes algorithm is meant to generate a smooth and continuous 3D surface out of discrete volumetric data, typically in the medical imaging, scientific visualization and 3D modeling fields. Here the resulting mesh appears in a solid form and this will aid in the internal structure of the data being understood and analyzed. Overall, this visualization demonstrates the way in which Marching Cubes

may be applied to 3D reconstruction to convert the points of volumetric data into a 3D shape that can be subsequently analyzed or visualized.

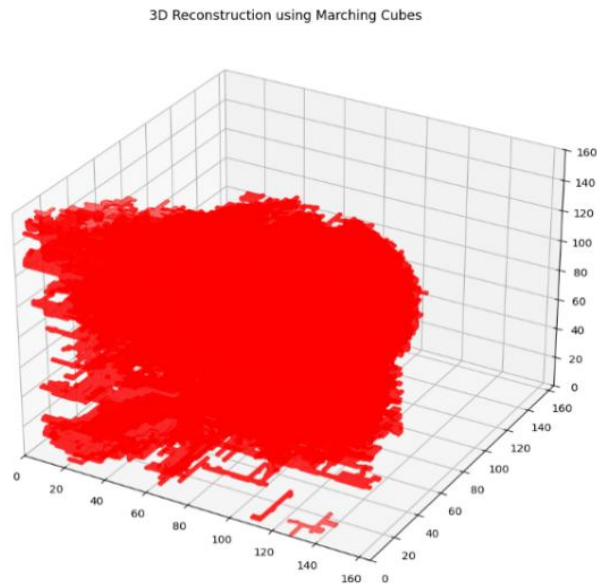


Figure 12: Cancer cell in breast image reconstructs with marching cubes algorithm

Secure data handling measures such as data anonymisation, encryption and access control were also necessary to guarantee the privacy and integrity of sensitive medical data utilized in this study. As table 4 and figure 10 illustrate, the capacity to guard the data greatly minimized the risk of unauthorized access to the data and exposure. The Unauthorized Access Detection Rate and Data Exposure rate had highly significant improvements ($p < 0.001$), which affirms that the measures implemented were very effective in securing patient data when processing and analysing patient data.

The effect of the strong security was also negligible on computational performance, including training time per epoch and memory usage, though resource consumption increased slightly (by about 2%). This proves that the presented framework is effective in balancing the data security with the computational efficiency and it can be used in real-time clinical applications, where both the security and the performance are the key aspects.

On the whole, the clinical applicability of the suggested model can be improved if secure data handling becomes successful since the sensitive patient data can be safely processed without limiting the performance of the breast cancer processing system. It proves that safe deep learning architectures can be deployed in medical imaging, and all regulations such as HIPAA or GDPR can be followed.

5 Conclusion

This research paper presents an automated deep learning software to detect breast cancer and reconstruct 3D tumors with NIFTI MRI data, with enhanced security data processing protocols. The major results indicate that the Hybrid UNet-ResNet model is superior in tumor segmentation with Dice coefficients of 0.68 to 0.79 and Jacquard indices of 0.51 to 0.65, which is more accurate in preserving tumor boundary. The statistical analysis provided significant gains in security and the Unauthorized Access Detection Rate and Data Exposure Rate improved by 100% ($p < 0.001$), which proves the effectiveness of the included privacy-saving measures. Although with such security measures, the effect of the security

measure was not strong and the training time and memory consumption increased by 2% which is not that high that the research has proven the effectiveness of the proposed framework in terms of being efficient and guaranteeing data safety. The results confirm the possibility of integrating safer data management in the medical imaging systems without any negative performance. In the future, the research might be directed towards maximizing the quality of localization of tumors through the incorporation of the state-of-the-art denoising methods and attention. Also, it can enhance the framework to take into account multi-modal imaging data and introduce GPU-based approaches to Marching Cubes to increase computational effectiveness and make the system more applicable to real-time clinical practice and faster and more accurate early detection of breast cancer.

References

- [1] Alagoz, O., Lowry, K. P., Kurian, A. W., Mandelblatt, J. S., Ergun, M. A., Huang, H., ... & from the CISNET Breast Working Group. (2021). Impact of the COVID-19 pandemic on breast cancer mortality in the US: estimates from collaborative simulation modeling. *JNCI: Journal of the National Cancer Institute*, 113(11), 1484-1494. <https://doi.org/10.1093/jnci/djab097>
- [2] Ben-Dror, J., Shalamov, M., & Sonnenblick, A. (2022). The history of early breast cancer treatment. *Genes*, 13(6), 960. <https://doi.org/10.3390/genes13060960>
- [3] Benitez Fuentes, J. D., Morgan, E., de Luna Aguilar, A., Mafra, A., Shah, R., Giusti, F., ... & Soerjomataram, I. (2024). Global stage distribution of breast cancer at diagnosis: a systematic review and meta-analysis. *JAMA oncology*, 10(1), 71-78. <https://doi.org/10.1001/jamaoncol.2023.4837>
- [4] Brackstone, M., Baldassarre, F. G., Perera, F. E., Cil, T., Chavez Mac Gregor, M., Dayes, I. S., ... & Eisen, A. F. (2021). Management of the axilla in early-stage breast cancer: Ontario Health (Cancer Care Ontario) and ASCO guideline. *Journal of Clinical Oncology*, 39(27), 3056-3082. <https://doi.org/10.1200/JCO.21.00934>
- [5] Burguin, A., Diorio, C., & Durocher, F. (2021). Breast cancer treatments: updates and new challenges. *Journal of personalized medicine*, 11(8), 808. <https://doi.org/10.3390/jpm11080808>
- [6] Burstein, H. J., Curigliano, G., Thürlimann, B., Weber, W. P., Poortmans, P., Regan, M. M., ... & Xu, B. (2021). Customizing local and systemic therapies for women with early breast cancer: the St. Gallen International Consensus Guidelines for treatment of early breast cancer 2021. *Annals of oncology*, 32(10), 1216-1235. <https://doi.org/10.1016/j.annonc.2021.06.023>
- [7] Debien, V., De Caluwé, A., Wang, X., Piccart-Gebhart, M., Tuohy, V. K., Romano, E., & Buisseret, L. (2023). Immunotherapy in breast cancer: an overview of current strategies and perspectives. *NPJ breast cancer*, 9(1), 7. <https://doi.org/10.1038/s41523-023-00508-3>
- [8] Derakhshan, F., & Reis-Filho, J. S. (2022). Pathogenesis of triple-negative breast cancer. *Annual Review of Pathology: Mechanisms of Disease*, 17, 181-204. <https://doi.org/10.1146/annurev-pathol-042420-093238>
- [9] Devericks, E. N., Carson, M. S., McCullough, L. E., Coleman, M. F., & Hursting, S. D. (2022). The obesity-breast cancer link: a multidisciplinary perspective. *Cancer and Metastasis Reviews*, 41(3), 607-625. <https://doi.org/10.1007/s10555-022-10043-5>
- [10] Dinapoli, L., Colloca, G., Di Capua, B., & Valentini, V. (2021). Psychological aspects to consider in breast cancer diagnosis and treatment. *Current oncology reports*, 23(3), 38. <https://doi.org/10.1007/s11912-021-01049-3>
- [11] German, R., Marino, N., Hemmerich, C., Podicheti, R., Rusch, D. B., Stiemsma, L. T., ... & Storniolo, A. M. (2023). Exploring breast tissue microbial composition and the association with breast cancer risk factors. *Breast Cancer Research*, 25(1), 82. <https://doi.org/10.1186/s13058-023-01677-6>

- [12] Goff, S. L., & Danforth, D. N. (2021). The role of immune cells in breast tissue and immunotherapy for the treatment of breast cancer. *Clinical breast cancer*, 21(1), e63-e73. <https://doi.org/10.1016/j.clbc.2020.06.011>
- [13] He, L., Li, F., Qin, Y., Li, Y., Hu, Q., Liu, Z., ... & Ai, T. (2025). Enhanced preoperative prediction of breast lesion pathology, prognostic biomarkers, and molecular subtypes using multiple models' diffusion-weighted MR imaging. *Scientific Reports*, 15(1), 4704. <https://doi.org/10.1038/s41598-024-81713-3>
- [14] Hong, R., & Xu, B. (2022). Breast cancer: an up-to-date review and future perspectives. *Cancer communications*, 42(10), 913-936. <https://doi.org/10.1002/cac2.12358>
- [15] Houghton, S. C., & Hankinson, S. E. (2021). Cancer progress and priorities: breast cancer. *Cancer epidemiology, biomarkers & prevention*, 30(5), 822-844. <https://doi.org/10.1158/1055-9965.EPI-20-1193>
- [16] Howard, F. M., & Olopade, O. I. (2021). Epidemiology of triple-negative breast cancer: a review. *The Cancer Journal*, 27(1), 8-16. <https://doi.org/10.1097/PPO.0000000000000500>
- [17] Hu, D., Li, Z., Zheng, B., Lin, X., Pan, Y., Gong, P., ... & Wang, L. (2022). Cancer-associated fibroblasts in breast cancer: Challenges and opportunities. *Cancer Communications*, 42(5), 401-434. <https://doi.org/10.1002/cac2.12291>
- [18] Jassim, G. A., Doherty, S., Whitford, D. L., & Khashan, A. S. (2023). Psychological interventions for women with non-metastatic breast cancer. *Cochrane Database of Systematic Reviews*, (1). <https://doi.org/10.1002/14651858.CD008729.pub3>
- [19] Katsura, C., Ogunmwonyi, I., Kankam, H. K., & Saha, S. (2022). Breast cancer: presentation, investigation and management. *British Journal of Hospital Medicine*, 83(2), 1-7. <https://doi.org/10.12968/hmed.2021.0459>
- [20] Lei, S., Zheng, R., Zhang, S., Wang, S., Chen, R., Sun, K., ... & Wei, W. (2021). Global patterns of breast cancer incidence and mortality: A population-based cancer registry data analysis from 2000 to 2020. *Cancer Communications*, 41(11), 1183-1194. <https://doi.org/10.1002/cac2.12207>
- [21] Rabiei, R., Ayyoubzadeh, S. M., Sohrabei, S., Esmaeili, M., & Atashi, A. (2022). Prediction of breast cancer using machine learning approaches. *Journal of biomedical physics & engineering*, 12(3), 297-308.
- [22] Rakha, E. A., Tse, G. M., & Quinn, C. M. (2023). An update on the pathological classification of breast cancer. *Histopathology*, 82(1), 5-16. <https://doi.org/10.1111/his.14786>
- [23] Sarhangi, N., Hajjari, S., Heydari, S. F., Ganjizadeh, M., Rouhollah, F., & Hasanzad, M. (2022). Breast cancer in the era of precision medicine. *Molecular biology reports*, 49(10), 10023-10037. <https://doi.org/10.1007/s11033-022-07571-2>
- [24] Swain, S. M., Shastry, M., & Hamilton, E. (2023). Targeting HER2-positive breast cancer: advances and future directions. *Nature reviews Drug discovery*, 22(2), 101-126. <https://doi.org/10.1038/s41573-022-00579-0>
- [25] Traves, K. P., & Sarah, E. H. (2021). Cokenakes. *Breast cancer treatment. American family physician*, 104(2), 171-178.
- [26] Turner, N. C., Oliveira, M., Howell, S. J., Dalenc, F., Cortes, J., Gomez Moreno, H. L., ... & Rugo, H. S. (2023). Capivasertib in hormone receptor-positive advanced breast cancer. *New England Journal of Medicine*, 388(22), 2058-2070. <https://doi.org/10.1056/NEJMoa2214131>
- [27] Wang, J., & Wu, S. G. (2023). Breast cancer: an overview of current therapeutic strategies, challenge, and perspectives. *Breast Cancer: Targets and Therapy*, 721-730. <https://doi.org/10.2147/BCTT.S432526>
- [28] Wu, J., Fan, D., Shao, Z., Xu, B., Ren, G., Jiang, Z., ... & Liao, N. (2022). CACA guidelines for holistic integrative management of breast cancer. *Holistic Integrative Oncology*, 1(1), 7. <https://doi.org/10.1007/s44178-022-00007-8>

- [29] Zhi, S., Chen, C., Huang, H., Zhang, Z., Zeng, F., & Zhang, S. (2024). Hypoxia-inducible factor in breast cancer: role and target for breast cancer treatment. *Frontiers in Immunology*, 15, 1370800. <https://doi.org/10.3389/fimmu.2024.1370800>
- [30] Zhu, Z., Wang, S. H., & Zhang, Y. D. (2023). A survey of convolutional neural network in breast cancer. *Computer modeling in engineering & sciences: CMES*, 136(3), 2127. <https://doi.org/10.32604/cmes.2023.025484>
- [31] Zubair, M., Wang, S., & Ali, N. (2021). Advanced approaches to breast cancer classification and diagnosis. *Frontiers in Pharmacology*, 11, 632079. <https://doi.org/10.3389/fphar.2020.632079>

Authors Biography



Manasa Sandeep is currently working as Assistant Professor in the Department of Computer Science and Engineering, Dayananda Sagar Academy of Technology and Management, Bengaluru. Her research interests include Computer Vision, Machine Learning, Security etc. She has obtained her B. E and M. Tech from VTU, Belagavi. She is currently pursuing Ph.D. from VTU, Belagavi. She has published several articles in peer-reviewed international journals and conferences.



Dr.C. Nandini is working as Professor and Head in the Department of Computer Science and Engineering, Dayananda Sagar Academy of Technology and Management, Bengaluru. She received her Ph.D. from VTU. Her research interests include Computer Vision, Cryptography and Network Security, Machine Learning, Artificial Intelligence and Intelligent Healthcare Systems. She has over 20 years of research experience and has supervised several doctoral students and has published extensively in reputed SCI-indexed journals. She has completed many funded research projects and also serves as a reviewer for various high-impact journals.